

# Nitrogen enhancement of GN-z11 by metal pollution from supermassive stars

S. Ebihara<sup>1</sup>, M. Fujii<sup>1</sup>, T. Saitoh<sup>2</sup>, Y. Hirai<sup>3</sup>, H. Umeda<sup>1</sup>, Y. Isobe<sup>4, 5, 6</sup>, and C. Nagele<sup>7</sup>

<sup>1</sup> Department of Astronomy, The University of Tokyo, 7-3-1 Hongo, Bunkyo-ku, Tokyo 113-0033, Japan

<sup>2</sup> Department of Planetology, Graduate School of Science, Kobe University, 1-1 Rokkodai-cho, Nada-ku, Kobe, Hyogo 657-8501, Japan

<sup>3</sup> Department of Community Service and Science, Tohoku University of Community Service and Science, 3-5-1 Iimoriyama, Sakata, Yamagata 998-8580, Japan

<sup>4</sup> Kavli Institute for Cosmology, University of Cambridge, Madingley Road, Cambridge, CB3 0HA, UK

<sup>5</sup> Cavendish Laboratory, University of Cambridge, 19 JJ Thomson Avenue, Cambridge, CB3 0HE, UK

<sup>6</sup> Waseda Research Institute for Science and Engineering, Faculty of Science and Engineering, Waseda University, 3-4-1, Okubo, Shinjuku, Tokyo 169-8555, Japan

<sup>7</sup> Department of Physics and Astronomy, Johns Hopkins University, Baltimore, MD 21218, USA

## ABSTRACT

**Context.** Spectroscopic observations by the James Webb Space Telescope (JWST) have revealed young, compact, high-redshift ( $z$ ) galaxies with high nitrogen-to-oxygen (N/O) ratios. GN-z11 at  $z = 10.6$  is one of these galaxies.

**Aims.** One possible scenario for such a high N/O ratio is pollution from supermassive stars (SMSs), from which stellar winds are expected to be nitrogen-rich. The abundance pattern is determined by both galaxy evolution and SMS pollution, but so far, simple one-zone models have been used. Using a galaxy formation simulation, we tested the SMS scenario.

**Methods.** We used a cosmological zoom-in simulation that includes chemical evolution driven by rotating massive stars (Wolf-Rayet stars), supernovae, and asymptotic giant branch stars. As a post-process, we assumed the formation of an SMS with a mass between  $10^3$  and  $10^5 M_{\odot}$  and investigated the contribution of its ejecta to the abundance pattern.

**Results.** The N/O ratio was enhanced by the SMS ejecta, and the abundance pattern of GN-z11, including carbon-to-oxygen and oxygen-to-hydrogen ratios, was reproduced by our SMS pollution model if the pollution mass fraction ranges within 10–30 per cent. Such a pollution fraction can be realized when the gas ionized by the SMS is polluted, and the gas density is  $10^4$ – $10^5 \text{ cm}^{-3}$  assuming a Strömgren sphere. We also compared the abundance pattern with those of other N/O-enhanced high- $z$  galaxies. Some of these galaxies can also be explained by SMS pollution.

**Key words.** Galaxies: ISM – Galaxies: evolution – Galaxies: individual: GN-z11 – ISM: abundances – Stars: evolution – Stars: mass-loss

## 1. Introduction

The James Webb Space Telescope (JWST) has revealed the existence of nitrogen-rich galaxies at high redshift ( $z$ ). A prime example of such galaxies is GN-z11. The galaxy was identified by the Hubble Space Telescope as having  $z = 11.09^{+0.08}_{-0.12}$  in Oesch et al. (2016), and recent JWST observation updated its redshift to  $z = 10.6$  (Bunker et al. 2023; Maiolino et al. 2024b). Several studies have reported that GN-z11 exhibits at least  $\log(\text{N/O}) > -0.5$  (Cameron et al. 2023; Isobe et al. 2023; Senchyna et al. 2024) from strong nitrogen lines in the rest-frame ultraviolet, regardless of whether a stellar or AGN radiation field is assumed. These nitrogen abundances are much higher than those of local galaxies (Pilyugin et al. 2012; Izotov et al. 2006; Berg et al. 2016, 2019), of which abundances correspond to the ejecta of core-collapse supernovae (CCSNe) (Nomoto et al. 2013; Watanabe et al. 2024). Such a high N/O ratio in some high- $z$  galaxies shows rather good agreement with that of globular clusters (GCs) in the Milky Way (Charbonnel et al. 2023; Senchyna et al. 2024; Ji et al. 2025).

According to the traditional stellar evolution scenario, oxygen is mainly enriched by CCSNe, whereas carbon and nitrogen are enriched by stellar winds from asymptotic giant branch (AGB)

stars. D’Antona et al. (2023) and McClymont et al. (2025) have suggested that AGB stars can be an origin of the N/O-enhanced gas of GN-z11. However, the main-sequence lifetimes of most progenitor stars (intermediate- or low-mass stars) are much longer than the age of high- $z$  galaxies, especially GN-z11, whose stellar age is estimated to be  $24^{+20}_{-10}$  Myr (Tacchella et al. 2023). On the other hand, Rizzuti et al. (2025) assumed an SN-driven galactic wind model that selectively blows oxygen away after CCSNe.

A possible source of nitrogen that could have been ejected early on is Wolf-Rayet (WR) stars. In WR stars, the CNO cycle enriches nitrogen. The stellar wind from WR stars can also explain the N/O ratio of GN-z11 (Isobe et al. 2023; Watanabe et al. 2024), but a fine-tuned star formation history is required (Cameron et al. 2023). Thus, Gunawardhana et al. (2025) claimed that the WR-only scenario can explain the carbon enrichment of GN-z11 but not its nitrogen excess. Tidal disruption events (TDEs) are also a possible scenario (Isobe et al. 2023). This scenario requires the existence of a supermassive black hole. GN-z11 may host an active galactic nucleus (AGN), but this remains under debate (Bunker et al. 2024; Maiolino et al. 2024b).

Another possible source is very massive stars (VMSs) and supermassive stars (SMSs). VMSs and SMSs are stars with  $10^3$ – $10^4$  and  $> 10^4 M_{\odot}$ , respectively. So far, no such massive stars have been observed, but they can be formed as Population (Pop) III stars (Latif et al. 2014; Chon et al. 2018; Latif et al. 2021; Hirano et al. 2021) or via runaway collisions of stars (Devecchi & Volonteri 2009; Sakurai et al. 2017; Fujii et al. 2024; Rantala et al. 2024). Although the evolution and yield of V/SMS have been little studied, Nagele & Umeda (2023) and Nandal et al. (2024) have proposed that V/SMS can also explain the N/O ratio of GN-z11 with V/SMS of stars with  $Z = 0.1 Z_{\odot}$  and Pop III stars, respectively. Hereafter, we refer to this V/SMS scenario simply as the SMS scenario.

Formation of SMSs during the formation of GN-z11-like galaxies would be expected from their compactness. The half-mass (half-light) radius of GN-z11 is measured to be only 200 pc (Tacchella et al. 2023). From the mass of  $10^9 M_{\odot}$ , the half-mass density of GN-z11 is estimated to be  $\sim 100 M_{\odot} \text{ pc}^{-3}$ . Assuming a power-law density distribution with a power of  $-2$ , we expect  $10^6 M_{\odot} \text{ pc}^{-3}$  at  $\sim 1 \text{ pc}$ . In star cluster formation simulations, such a high density is shown to result in runaway collision of stars (Portegies Zwart & McMillan 2002) and the formation of V/SMSs (Fujii et al. 2024; Rantala et al. 2024). In addition, the N/O-enhanced population is also known in GCs in the Milky Way (Charbonnel et al. 2023), and V/SMSs have also been suggested for GCs (Gieles et al. 2018). Thus, SMS formation in GN-z11-like galaxies seems to be a natural consequence.

Previous numerical studies of N-enrichment due to SMSs have been performed using one-zone models (Fukushima et al. 2025; Watanabe et al. 2024). However, real galaxies are formed through more complicated dynamical and chemical evolution. Saitoh et al. (2025) performed a numerical simulation of galaxy formation similar to GN-z11. The simulation showed that N/O is enriched during the first 10–20 Myr after a bursty star formation due to the stellar winds from rotating massive stars, although the N/O ratio was slightly lower than that of the observational lower limit of GN-z11. Since their simulation did not include SMSs, it remains unclear whether SMSs are responsible for the observed level of N-enrichment under the realistic environments of galaxy formation.

In this paper, we test the SMS scenario using the cosmological simulation results performed in Saitoh et al. (2025). From the dynamical evolution of the galaxy, we can assume the formation of SMSs as a post-process. In contrast to previous studies using one-zone models (Fukushima et al. 2025; Watanabe et al. 2024), our 3D-model can trace a spacial distribution of GN-z11-like galaxies, thereby providing a more realistic chemical and dynamical evolution.

This paper consists of the following sections. In Section 2, the calculation code and the setup of our galaxy formation simulation are described. Section 3 states the results of our simulation and shows how our SMS scenario can realize chemical abundances similar to those of GN-z11. In Section 4, we discuss whether SMS scenario can explain other N/O-enhanced galaxies. We summarize our research in Section 5.

## 2. Method

### 2.1. Numerical simulation

We adopt the simulation results presented in Saitoh et al. (2025). Hereafter, we briefly summarize the simulation. The simulation was performed using a zoom-in technique for a halo taken from a cosmological structure formation simulation. The tar-

get halo is the most massive one in a  $100 h^{-1} \text{Mpc}^3$  volume at  $z \sim 10$ . Its mass is comparable to the expected mass of GN-z11 (Scholtz et al. 2024). Using MUSIC (Hahn & Abel 2011), the initial condition was generated assuming a standard cosmological parameters with Planck Collaboration et al. (2020) ( $H_0 = 67.32$ ,  $\Omega_M = 0.3158$ ,  $\Omega_{\Lambda} = 0.6842$ ,  $\Omega_b = 0.04938$ , and  $\sigma_8 = 0.812$ ). The mass resolutions of  $4628 M_{\odot}$  and  $24972 M_{\odot}$  for baryons and dark matter, respectively, for the zoomed-in region. The softening lengths are  $\epsilon_{\text{baryon}} = 5.7 \text{ pc}$  and  $\epsilon_{\text{DM}} = 12.6 \text{ pc}$  for baryons and dark matter, respectively. The boundary particles have larger masses and softening lengths than those in the zoomed-in region.

The cosmological zoom-in simulation was performed using ASURA (Saitoh et al. 2008, 2009), which is a parallel  $N$ -body/smoothed particle hydrodynamics (SPH) code that solves gravitational interactions with the Tree method (Barnes & Hut 1986) and models hydrodynamical interactions with the density-independent formulation of SPH (Saitoh & Makino 2013, 2016). GRACKLE (Smith et al. 2017) is used to evaluate radiative cooling and heating of gas, directly solving the evolution of 12 species while using pre-computed tables for metal cooling and heating constructed by CLOUDY (Ferland et al. 2013). Ultraviolet background from (Haardt & Madau 2012) and Lyman-Werner background from (Incatasciato et al. 2023) are included as external radiation fields.

Star formation is implemented based on a simple stellar population (SSP) approximation. A gas particle forms a star particle with an efficiency of  $C_* = 0.5$  when it satisfies the following conditions: (i) high density ( $n_{\text{H}} > 10^3 \text{ cm}^{-3}$ ), (ii) low temperature ( $T < 100 \text{ K}$ ), and (iii) converging flow ( $\nabla \cdot \mathbf{v} < 0$ ). For higher-metallicity stars ( $Z > 10^{-5} Z_{\odot}$ ), SSP particles follow the Chabrier initial mass function (IMF) (Chabrier 2003) with a mass range of  $0.1$ – $100 M_{\odot}$ , while for low-metallicity stars ( $Z < 10^{-5} Z_{\odot}$ ), the Susa IMF (Susa et al. 2014) with a mass range of  $0.7$ – $300 M_{\odot}$  is used.

Stellar evolution and feedback are handled with CELIB (Saitoh 2017), including four chemical enrichment processes: stellar winds from rotating massive stars, CCSNe, AGB mass loss, and Type Ia SNe. Yield tables from Limongi & Chieffi (2018), Nomoto et al. (2013), the FRUITY database (Domínguez et al. 2011; Cristallo et al. 2014, 2015, 2016), and Seitenzahl et al. (2013) are used for these processes. The momentum feedback model of Hopkins et al. (2018) is applied, with CCSNe releasing  $10^{51}$ – $10^{52} \text{ erg}$ . Metal diffusion driven by turbulence (Shen et al. 2010) is taken into account, with a diffusion coefficient of 0.01 (Hirai & Saitoh 2017).

The output interval of the original simulation of Saitoh et al. (2025) is insufficient to measure the role of SMSs. Hence, we run a new simulation starting from the output at  $z \sim 11.2$  (the corresponding cosmic age is 402 Myr) with an output interval of 1.38 Myr. While the overall evolution remains consistent with the original simulation, we observe slight differences in, e.g., the star formation rate and the absolute values of chemical composition due to the numerical fluctuations.

### 2.2. Supermassive star models

The chemical yields of the SMSs considered in this paper were taken from the stellar evolution and hydrodynamical simulations of Nagele & Umeda (2023). They first performed stellar evolution simulations for  $10^3$ ,  $10^4$ ,  $5 \times 10^4$ , and  $10^5 M_{\odot}$  SMS models using a post-Newtonian stellar evolution code, HOSHI (Takahashi et al. 2016, 2018, 2019; Yoshida et al. 2019; Nagele et al. 2020). These models included mass loss due to line-driven winds, and the enriched material in these winds is in part the source of the chemical

yields. Strictly speaking, a star with  $10^3 M_\odot$  probably should be classified as a VMS, but for simplicity we will refer to all four models as SMSs. The HOSHI code solves the hydrodynamical equations and heat dispersion under the 1D stellar structure via the Henyey method. HOSHI includes a nuclear reaction network of 52 isotopes (including the CNO cycle), neutrino cooling, convection, mass loss, and rotation.

After the stellar evolution simulations were completed, they performed a GR stability analysis (Nagele et al. 2022, 2023) on each time snapshot of the stellar evolution simulations. SMSs are radiation-dominated and, as such, they are vulnerable to collapse induced by the general relativistic radial instability (Chandrasekhar 1964). This is not necessarily the only instability that can destabilize these stars, but it is thought to be the first one to activate during their evolution. The stability analysis developed in (Nagele et al. 2022) involves solving for the frequency of oscillations of a perturbed SMS, which can be done for a set of hydrostatic stellar properties. If the frequency squared is less than zero, the perturbation will induce exponential motion as opposed to sinusoidal, and the star will collapse.

This point of collapse is obviously the end of the star's lifetime, but in order to define a stellar age, we need the starting point of the star's lifetime. There is no obvious zero-age main-sequence point for massive stars. Therefore, here we define the start of the SMS life as occurring at  $\log T_c = 7.5$ . Given this definition, the stellar lifetimes are 1.7, 1.6, 1.3, 0.65 Myr for  $M = 10^3, 10^4, 5 \times 10^4, 10^5 M_\odot$ , respectively. Fig. 1 shows the effective temperature as a function of time after this initial time for the  $10^4 M_\odot$  SMS model. The maximum effective temperature was  $T_{\text{eff}} = 7.09 \times 10^4$  K and the radius at that moment  $124 R_\odot$ . Unlike accreting SMSs (Haemmerlé et al. 2019; Nagele & Umeda 2024), the models considered here are relatively compact with higher surface temperatures.

Once the GR radial instability is found in a given evolutionary snapshot, the authors transferred that snapshot into a Lagrangian 1D GR hydrodynamics code coupled to a large nuclear network (Yamada 1997; Takahashi et al. 2016; Nagele et al. 2020, 2022, 2023). Running this code determined whether the unstable star would collapse or explode due to nuclear burning (in this case, the CNO cycles and proton captures of other light elements). The yields discussed in this paper consist of the material in the winds from the evolutionary calculation, in addition to any material that is unbound during a pulsation or explosion.

During the evolutionary simulation, the two heavier models,  $5 \times 10^4$  and  $10^5 M_\odot$ , became GR unstable around the helium burning phase. The two lower mass models,  $10^3$  and  $10^4 M_\odot$ , remained stable during helium burning and finally formed carbon-oxygen cores. Extreme convection dredging up helium, carbon, and oxygen from the core meant that the surfaces of these stars (and hence the composition of the winds) contained super-solar abundances of carbon and oxygen, and this is in contrast to the heavier models which were more nitrogen dominated. Thus, the stability of the star into different nuclear burning stages affects the character of the *total* yields that star produces.

In Table 1, we summarize the yields of each SMS model, as given in Table 1 of Nagele & Umeda (2023). Comparing the four models, the  $10^3$ ,  $10^4$ , and  $5 \times 10^4 M_\odot$  models have higher oxygen than carbon and nitrogen. For these three models, the ratio of nitrogen to oxygen is highest for  $5 \times 10^4 M_\odot$ , which does not reach the late helium burning phase. Nitrogen is also higher than carbon in all three models. The  $10^5 M_\odot$  model has larger carbon and nitrogen than oxygen, and this comes primarily from the thermonuclear explosion, which produces large amounts of carbon and nitrogen (Table 1). The overall amount of CNO

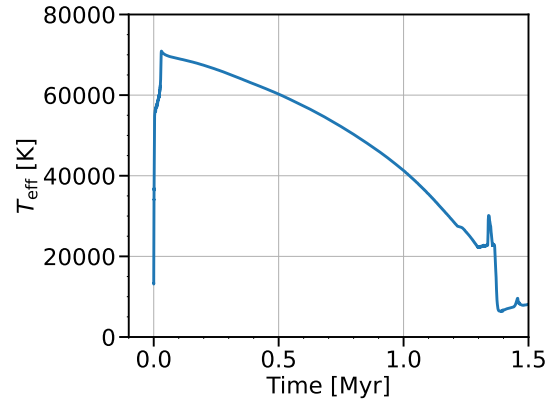


Fig. 1: The effective temperature evolution of  $10^4 M_\odot$  SMS model performed in Nagele & Umeda (2023).

elements is similar to the lower mass models, however, due to this model's collapse earlier in its evolution, meaning the total mass lost to winds is lower.

### 3. Results

#### 3.1. Galaxy formation

We present the evolution of the projected surface density of each component (stars, gas, and dark matter) in Fig. 2. As shown in these snapshots, the galaxy evolved via mergers of three dark matter clumps between  $z = 11.20$  and  $z = 10.77$ . One of the merging dark matter clumps brought gas into the main halo (see the clump at lower left in the  $\Sigma_{\text{DM}}$  figure at  $z = 11.20$ ). Such gas accretion triggered star formation.

The time evolution of the mass of our simulated galaxy is shown in Fig. 3. Here, we define the mass within 1 kpc from the galactic center as the mass of the galaxy. Note that the galactic center was determined using AHF, considering the density of dark matter and baryons. The dark matter mass was almost constant ( $10^{9.5} M_\odot$ ) between 410 and 470 Myr. On the other hand, the gas mass rapidly increased from  $\sim 420$  Myr. As a result, the stellar mass also rapidly increased after  $\sim 420$  Myr ( $z = 10.80$ ). At this moment, the mergers of the three dark-matter clumps occurred (see Fig. 2). The stellar mass reached  $\sim 10^8 M_\odot$  until  $z = 10.60$ . This value is still slightly smaller than the observationally estimated stellar mass of GN-z11;  $\log(M_*/M_\odot) = 8.7 \pm 0.06$  (Bunker et al. 2024) or  $\log(M_*/M_\odot) = 9.1_{-0.4}^{+0.3}$  (Tacchella et al. 2023).

The star formation slightly slows down after  $z = 10.60$  but continues until 470 Myr. The stellar mass finally reached  $10^9 M_\odot$ , which is comparable to GN-z11. Although the stellar mass at  $z = 10.60$  is slightly lower than that of GN-z11, we assume that an SMS formed around this time, as it is just after the rapid increase in stellar mass. Previous numerical studies on star cluster formation suggested that an SMS can be formed via runaway collisions during a rapid star formation of the system (Fujii et al. 2024; Rantala et al. 2024).

We also measured the star formation rate (SFR) of the central region (10 pc) of this galaxy because stellar collisions are expected to occur at the galactic center. For each snapshot, we identified star particles within 10 pc of the galactic center. From the formation-epoch data for each star particle, we calculated the SFR in bins of  $10^4$  yr between the target snapshot and the previous one. Repeating this for each snapshot, we constructed the SFR history, as shown in Fig. 4. The SFR was fluctuating around

Table 1: Stellar masses, properties, and yields (hydrogen, helium, carbon, nitrogen, and oxygen) of SMSs from Table 1 in [Nagele & Umeda \(2023\)](#).

| $M_{\text{SMS}}$<br>[ $M_{\odot}$ ] | Enrichment source | $E_{\text{explosion}}$<br>[erg] | H<br>[ $M_{\odot}$ ] | He<br>[ $M_{\odot}$ ] | C<br>[ $M_{\odot}$ ] | N<br>[ $M_{\odot}$ ] | O<br>[ $M_{\odot}$ ] |
|-------------------------------------|-------------------|---------------------------------|----------------------|-----------------------|----------------------|----------------------|----------------------|
| $10^3$                              | wind              | —                               | 205                  | 334                   | 9.91                 | 17                   | 27                   |
| $10^4$                              | wind              | —                               | $1.65 \times 10^3$   | $2.73 \times 10^3$    | 1.81                 | 75.8                 | 133                  |
| $5 \times 10^4$                     | wind              | —                               | $5.06 \times 10^3$   | $2.7 \times 10^3$     | 0.142                | 6.69                 | 0.412                |
| $10^5$                              | wind/explosion    | $7.97 \times 10^{54}$           | $4.19 \times 10^4$   | $5.8 \times 10^4$     | 5.63                 | 81.4                 | 0.884                |

$10 M_{\odot} \text{ yr}^{-1}$  between  $z = 10.77$  and  $z = 10.60$ . The SFR reached the peak,  $> 10 M_{\odot} \text{ yr}^{-1}$ , between  $z = 10.67$  and  $z = 10.65$ . In [Fujii et al. \(2024\)](#), the SFRs of their star clusters were typically  $\sim 1 M_{\odot} \text{ yr}^{-1}$  and reached  $\sim 10 M_{\odot} \text{ yr}^{-1}$  for the most massive ones, and their star clusters resulted in the formation of stars with  $> 10^3 M_{\odot}$ . Given this discussion, we assume that SMS was formed between  $z = 10.77$  and  $z = 10.60$  through runaway collisions triggered by rapid star formation. Hereafter, we focus on the  $z = 10.77\text{--}10.60$  snapshots to investigate the pollution of the formed SMS.

In Fig. 5, we present the density profiles of the gas, star, and dark matter at  $z = 10.65$ , when the SFR reached its peak. For reference, we draw shaded regions for each component from the same density profiles between  $z = 10.77$  and  $z = 10.60$ . At  $z = 10.77$ , the stellar mass was comparable to the gas mass at the galactic center, but at  $z = 10.65$  and later, stars were dominant compared to the gas. This is because accreting gas was consumed by rapid star formation. In the central region, baryons dominate dark matter.

In addition, we calculated the mass-weighted mean age of stars within  $10 \text{ pc}$  of the galactic center at  $z = 10.60$ , which was  $5.05 \text{ Myr}$ . As the lifetime of  $> 10 M_{\odot}$  stars is set to be  $< 100 \text{ Myr}$  in CELIB, our galaxy has already been enriched by WR at this moment, but the pollution from AGB stars has not been activated yet.

Assuming that the observed lines come from the high-temperature gas ionized by the SMS at the galactic center, we focus on the chemical abundance of the gas within  $10 \text{ pc}$  from the galactic center. As summarized in Table 2, we measured the abundance ratios of H, C, N, O, and He. The abundance ratio among C, N, and O had a range of  $\log(\text{N/O}) = -1.81\text{--}-0.90$ ,  $\log(\text{C/O}) = -0.65\text{--}-0.05$  for  $z = 10.77\text{--}10.60$ . On the other hand, O/H and He/H little changed in the same time range,  $12 + \log(\text{O/H}) = 7.83\text{--}7.86$ , and  $\text{He/H} = 0.083\text{--}0.089$ .

Hereafter, we describe the observed abundance ratios of GN-z11 used for comparison with our simulations. In this paper, we primarily adopt observed O/H and C/O values of GN-z11 ([Isobe et al. 2025](#)) based on the latest JWST data ([Bunker et al. 2023; Maiolino et al. 2024a,b; Álvarez-Márquez et al. 2025](#)) and two assumptions of electron number densities of  $n_e = 10^3$  and  $10^5 \text{ cm}^{-3}$ . For N/O and He/H values, which have not yet been reported by [Isobe et al. \(2025\)](#), we refer to measurements from other studies ([Cameron et al. 2023; Ji et al. 2025](#)) that assume a low  $n_e$  value of  $100 \text{ cm}^{-3}$ . We confirm that all three studies report/assume consistent electron temperatures and O/H for the low-density case of [Isobe et al. \(2025\)](#). We summarized these values in Table 2. For comparison, the solar abundance ([Asplund et al. 2021](#)) is given in the table.

Without SMS pollution, the N/O was smaller than that of GN-z11 and even comparable with the solar abundance when  $z =$

10.60, although the pollution from WR stars (massive rotating stars) has already started in our simulation. On the other hand, the C/O of our simulation matched the observed value when  $z \simeq 10.70$ , but it exceeded the observed value at later times. The O/H of our simulation was close to the observed values assuming  $n_e = 10^3 \text{ cm}^{-3}$ .

### 3.2. SMS formation

Recent numerical simulations have suggested that SMSs form via runaway collisions of stars during the formation of star clusters ([Fujii et al. 2024; Rantala et al. 2024](#)). The central density necessary for runaway collisions is typically  $10^6 M_{\odot} \text{ pc}^{-3}$ . As shown in Fig. 5, the density of the stellar component is slightly less than  $10^6 M_{\odot} \text{ pc}^{-3}$ . In our simulation, however, the softening length for baryons is  $5.7 \text{ pc}$ , and therefore, we cannot resolve the density in the innermost region of this galaxy. If this density profile continues into the inner region beyond  $1 \text{ pc}$ , we expect the central stellar density to reach  $10^6 M_{\odot} \text{ pc}^{-3}$ . In the following, we estimate the SMS mass that can be formed in this galaxy.

From the results of star cluster formation simulations resolving individual stars, [Fujii et al. \(2024\)](#) suggested that 3–5 per cent of the formed stars contributed to the SMSs through runaway collisions; in other words, the mass increase rate of SMSs in star clusters or galaxies is estimated to be 3–5 per cent of the SFR of the host system. Using this relation, we estimated the SMS growth rate from the SFR of the central region of the galaxy. In the previous subsection, we measured the SFR of the central region of our simulated galaxy (see Fig. 4). We assumed that stars within the central  $10 \text{ pc}$  of the galaxy could participate in runaway collisions.

As shown in Fig. 4, the SFR increases and decreases due to the mass accumulation history of the galaxy. It also fluctuates with time. In our simulation, the SFR was always larger than  $3 \times 10^{-1} M_{\odot} \text{ yr}^{-1}$  after the first peak of the star formation at  $z \simeq 10.77$ . On the other hand, the maximum star formation rate achieved during the simulation was  $30 M_{\odot} \text{ yr}^{-1}$  at  $z \simeq 10.67$ . Combining this SFR with the efficiency of the runaway collision, 3–5 per cent of the formed stellar mass, we can estimate the maximum/minimum mass increase rate of SMS. The lower limit of the mass increase rate of SMS is calculated to be 3 per cent of  $3 \times 10^{-1} M_{\odot} \text{ yr}^{-1}$ , i.e.,  $9 \times 10^{-3} M_{\odot} \text{ yr}^{-1}$ . Similarly, the maximum mass increase rate is calculated to be 5 per cent of  $30 M_{\odot} \text{ yr}^{-1}$ , i.e.,  $1.5 M_{\odot} \text{ yr}^{-1}$ .

Following [Fujii et al. \(2024\)](#) and [Pacucci et al. \(2025\)](#), we assumed a constant mass increase rate. For the mass loss rate, we adopted one depending on the VMS mass ( $M_{\text{VMS}}$ ) and metallicity

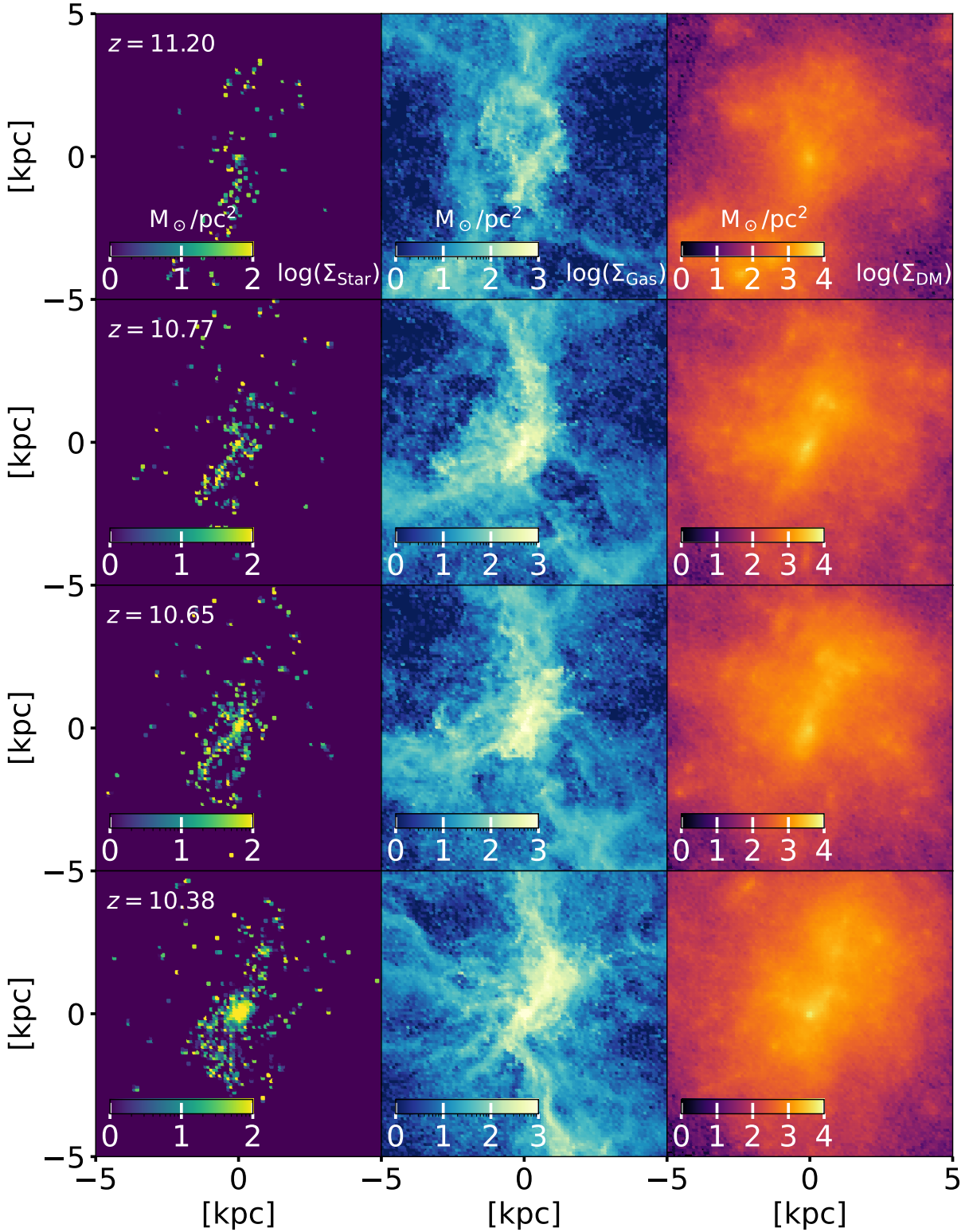


Fig. 2: Projected surface densities of stars (left), gas (middle), and dark matter (right) at  $z = 11.20, 10.77, 10.65$ , and  $10.38$  from top to bottom.

(Z) ([Vink 2018](#)):

$$\log \dot{M}_{\text{VMS}} = -9.13 + 2.1 \log(M_{\text{VMS}} / M_{\odot}) + 0.74 \log(Z/Z_{\odot}) \quad [\text{M}_{\odot} \text{ yr}^{-1}]. \quad (1)$$

As the metallicity ( $Z$ ) of VMS, we adopted that of the gas within 10 pc from the galactic center,  $1.37 \times 10^{-3}$  at  $z = 10.65$ , which is  $\bar{Z} \simeq 0.1 Z_{\odot}$  assuming the solar metallicity of  $Z_{\odot} = 0.0134$  ([Asplund et al. 2009](#)).

Assuming a constant mass increase rate, the mass loss and mass increase rates balance at a certain VMS mass because

Table 2: Chemical abundance ratios of our simulated galaxy, the sun, GN-z11, and other N/O-enhanced  $z \gtrsim 6$  galaxies summarized in [Ji et al. \(2025\)](#).

| Name  | Redshift | $\log(\text{N/O})$      | $\log(\text{C/O})$      | $12 + \log(\text{O/H})$ | $\text{He/H}$             | Reference |
|---|----------|-------------------------|-------------------------|-------------------------|---------------------------|-----------|
| Our result                                    | 10.77    | -1.81                   | -0.65                   | 7.83                    | 0.083                     | -         |
|   | 10.65    | -1.32                   | -0.38                   | 7.82                    | 0.085                     | -         |
|   | 10.60    | -0.90                   | -0.05                   | 7.86                    | 0.089                     | -         |
| Sun   | -        | -0.86                   | -0.23                   | 8.69                    | 0.082                     | (1)       |
| GN-z11 (Fiducial, $T_e = 1.46 \times 10^4$ K) | 10.6     | $> -0.25$               | $> -0.78$               | $7.82 \pm 0.2$          | -                         | (2)       |
| GN-z11 ( $n_e = 10^3 \text{ cm}^{-3}$ )       | 10.6     | -                       | $-0.61^{+0.07}_{-0.09}$ | $7.87^{+0.19}_{-0.16}$  | -                         | (3)       |
| GN-z11 ( $n_e = 10^5 \text{ cm}^{-3}$ )       | 10.6     | -                       | $-0.64^{+0.07}_{-0.08}$ | $8.37^{+0.19}_{-0.15}$  | -                         | (3)       |
| GN-z11  | 10.6     | -                       | -                       | -                       | $0.073^{+0.046}_{-0.029}$ | (4)       |
| ID397   | 6.00     | $-0.67^{+0.14}_{-0.13}$ | -                       | $7.96^{+0.10}_{-0.08}$  | -                         | (5)       |
| RXJ2248-ID                                    | 6.11     | $-0.39^{+0.10}_{-0.08}$ | $-0.83^{+0.11}_{-0.10}$ | $7.43^{+0.17}_{-0.09}$  | $0.166^{+0.018}_{-0.014}$ | (6)       |
| GLASS_150008                                  | 6.23     | $-0.40^{+0.05}_{-0.07}$ | $-1.08^{+0.06}_{-0.14}$ | $7.65^{+0.14}_{-0.08}$  | $0.142 \pm 0.054$         | (7)       |
| A1703-zd6                                     | 7.04     | $-0.6 \pm 0.3$          | $-0.74 \pm 0.18$        | $7.47 \pm 0.19$         | -                         | (8)       |
| A1703-zd6                                     | 7.04     | -                       | -                       | -                       | $0.082 \pm 0.017$         | (4)       |
| GN-z8-LAE                                     | 8.28     | $-0.44 \pm 0.36$        | $-0.69 \pm 0.21$        | $7.85 \pm 0.17$         | -                         | (9)       |
| CEERS_01019 (SF)                              | 8.68     | $> 0.28$                | $< -1.04$               | $7.94^{+0.46}_{-0.31}$  | -                         | (4)       |
| GN-z9p4                                       | 9.38     | $-0.59 \pm 0.24$        | $< -1.18$               | $7.38 \pm 0.15$         | -                         | (10)      |
| GS-z9-0                                       | 9.43     | $-0.93 \pm 0.37$        | $-0.90 \pm 0.26$        | $7.49^{+0.11}_{-0.15}$  | -                         | (11)      |
| GHZ9  | 10.15    | $-0.08-0.12$            | $-0.96-0.45$            | $6.69-7.69$             | -                         | (12)      |
| GHZ2  | 12.34    | $-0.25 \pm 0.05$        | $-0.74 \pm 0.20$        | -                       | -                         | (13)      |
| GHZ2  | 12.34    | -                       | -                       | $7.44^{+0.26}_{-0.24}$  | -                         | (14)      |
| MoM-z14                                       | 14.44    | $-0.57^{+0.28}_{-0.45}$ | $-0.91^{+0.39}_{-0.22}$ | $7.33^{+0.65}_{-0.56}$  | -                         | (15)      |

References: (1) [Asplund et al. \(2021\)](#); (2) [Cameron et al. \(2023\)](#); (3) [Isobe et al. \(2025\)](#); (4) [Ji et al. \(2025\)](#); (5) [Stiavelli et al. \(2025\)](#); (6) [Topping et al. \(2024\)](#); [Yanagisawa et al. \(2024\)](#); (7) [Isobe et al. \(2023\)](#); [Yanagisawa et al. \(2024\)](#); (8) [Topping et al. \(2025\)](#); (9) [Navarro-Carrera et al. \(2024\)](#); (10) [Schaerer et al. \(2024\)](#); (11) [Curti et al. \(2025\)](#); (12) [Napolitano et al. \(2025\)](#); (13) [Castellano et al. \(2024\)](#); (14) [Calabro et al. \(2024\)](#); (15) [Naidu et al. \(2025\)](#).

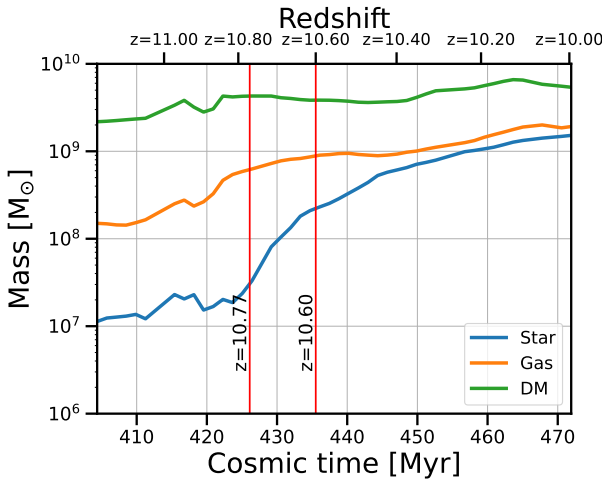


Fig. 3: Mass evolution of stars (blue), gas (orange), and dark matter (green) within 1 kpc from the galactic center. Redshifts of each snapshot are noted above the upper  $x$  axis. The red vertical lines indicate the moment of  $z = 10.77$  and  $z = 10.60$ .

the mass loss rate increases with VMS mass. With the minimum mass increase rate ( $9 \times 10^{-3} \text{ M}_\odot \text{ yr}^{-1}$ ), the SMS mass

converged to  $5.0 \times 10^3 \text{ M}_\odot$  (see Fig. A.1). In this case, the formation timescale was  $\sim 1$  Myr, which is sufficiently shorter than the lifetime of SMSs (see Fig. 1). With the maximum mass increase rate ( $1.5 \text{ M}_\odot \text{ yr}^{-1}$ ), in contrast, the SMS mass converged to  $5.7 \times 10^4 \text{ M}_\odot$  (see Fig. A.2), and the formation time was only 0.1 Myr. Thus, we estimated  $5 \times 10^3-6 \times 10^4 \text{ M}_\odot$  as the SMS mass range which can be formed at the galactic center.

### 3.3. Abundance pattern with SMS pollution

In Fig. 6, we present the abundance ratios of C, N, O, and H of the gas within 10 pc from the galactic center between  $z = 10.77$  and 10.60 obtained from our galaxy formation simulation. From  $z = 10.77$  to 10.60, both the N/O and C/O increased with time and at  $z = 10.60$ , reached their maximum values (see also [Saitoh et al. 2025](#)).

For comparison, we also plotted the abundance patterns of GN-z11 obtained from observational estimations summarized in Table 2. As we mentioned in section 3.1, [Cameron et al. \(2023\)](#) adopted an electron temperature  $T_e = 1.46 \times 10^4$  K as a fiducial one. [Isobe et al. \(2025\)](#) showed O/H and C/O assuming an electron number density  $n_e = 10^3 \text{ cm}^{-3}$  and  $10^5 \text{ cm}^{-3}$ . As shown in Fig. 6 and Table 2, the N/O ratio of this galaxy is lower than that of GN-z11 without SMSs.

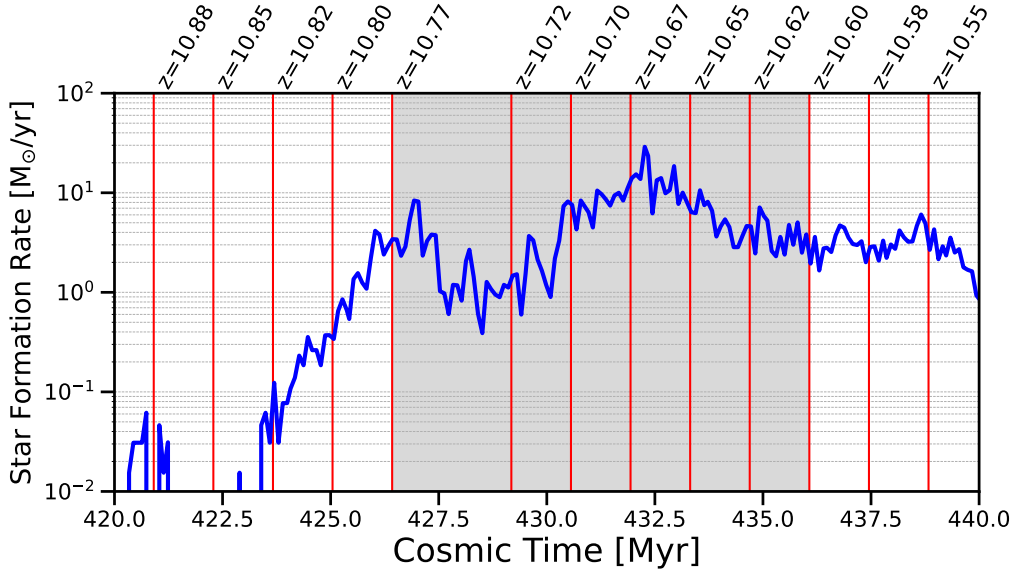


Fig. 4: Time evolution of the star formation rate in the central region (within 10 pc) of our simulated galaxy. Red vertical lines indicate the timing of the snapshots. Redshifts of each snapshot are noted above the upper  $x$  axis. The shaded region indicates the time range between  $z = 10.77$  and  $10.60$ .

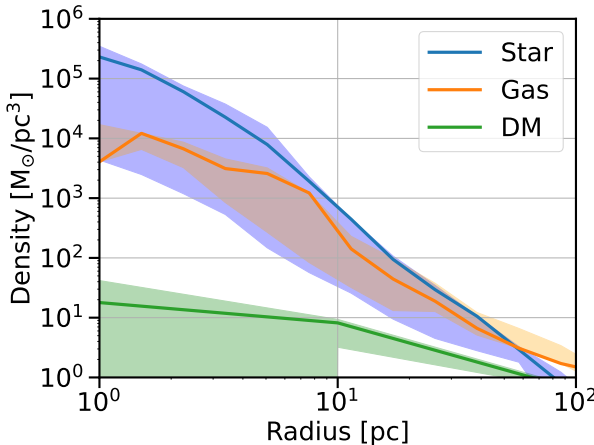


Fig. 5: Radial density profiles of dark matter (green), gas (orange), and stars (blue) at  $z = 10.65$ . The shaded regions indicate the possible value ranges of each component during  $z = 10.77$ – $10.60$ .

In the same plot, we also show the abundance pattern obtained by adding the ejecta from each SMS model. Similar to [Nagele & Umeda \(2023\)](#), we show the abundance pattern changing the fraction of the mass from the SMS ejecta. Here, we define the pollution fraction due to SMS ejecta ( $f_{\text{SMS}}$ ) as

$$f_{\text{SMS}} = \frac{M_{\text{ej}}}{M_{\text{ej}} + M_{\text{gas}}}, \quad (2)$$

where  $M_{\text{ej}}$  is the ejecta mass of the SMS and  $M_{\text{gas}}$  is the gas mass which is in the galaxy and polluted by the SMS ejecta. As shown in the figure, the  $5 \times 10^4$  and  $10^5 M_{\odot}$  SMS models at  $z = 10.77$  can reproduce the observed GN-z11 abundance pattern when  $f_{\text{SMS}} \simeq 30$  per cent. The observed O/H depends on the assumed electron number density. For the  $5 \times 10^4$  and  $10^5 M_{\odot}$  models,  $n_e = 10^3 \text{ cm}^{-3}$  was consistent with the observation. On the other hand, the  $10^4 M_{\odot}$  model at  $z = 10.60$  can also reach

the abundance pattern of GN-z11, when  $f_{\text{SMS}} \simeq 10$  per cent. The O/H value mixed with the  $10^4 M_{\odot}$  SMS model matched the O/H obtained with  $n_e = 10^5 \text{ cm}^{-3}$ .

Hereafter, we estimate  $f_{\text{SMS}}$  assuming that (1) the radiation/explosion from the SMS forms an HII region and (2) the ejecta from the SMS pollute the gas in it. We assume that the SMS ionizes the surrounding gas and forms an HII region, and the gas in the HII region is fully mixed with the SMS ejecta. As we mentioned above, we estimated the SMS mass formed in this galaxy is  $5 \times 10^3$ – $6 \times 10^4 M_{\odot}$ . Because the  $10^3$ ,  $10^4$ , and  $5 \times 10^4 M_{\odot}$  SMS models do not explode as supernovae (see Table 1), we estimate the size and mass of the HII region using the stellar temperature and radius of the  $10^4 M_{\odot}$  SMS model (see Sec. 2.2).

As shown in Table 1,  $10^3$ ,  $10^4$ , and  $5 \times 10^4 M_{\odot}$  SMS models do not result in supernovae. Thus, we assumed that these SMSs formed the Strömgren sphere under a uniform gas density at the galactic center. In real galaxies, however, gas distribution is hardly uniform. As shown in Fig. 5, the gas distribution in the central region is not uniform on a 10 pc scale. In general, the geometry of ionized regions is non-spherical. If gas density at the center of GN-z11 is not uniform, the Strömgren radius can lengthen in a direction that gas is optically-thin. Considering the inhomogeneity of the gas distribution, the  $f_{\text{SMS}}$  could also vary from a few to a few 10 per cent. Observationally, [Álvarez-Márquez et al. \(2025\)](#) suggested that the ionized radius of GN-z11 is  $\simeq 64$  pc, and [Xu et al. \(2024\)](#) estimated CIII] emission's half light radius is  $\sim 300$  pc, although the observational resolution is not sufficiently high to resolve 10 pc scale.

For the size of the HII region, we adopt Strömgren radius ( $R_S$ ; [Strömgren 1939](#)):

$$R_S = \left( \frac{3Q}{4\pi n_{\text{H}}^2 \alpha} \right)^{1/3}, \quad (3)$$

where  $Q$  is an ionizing photon production rate of the SMS,  $n_{\text{H}}$  is a number density of neutral hydrogen atoms, and  $\alpha$  is a recom-

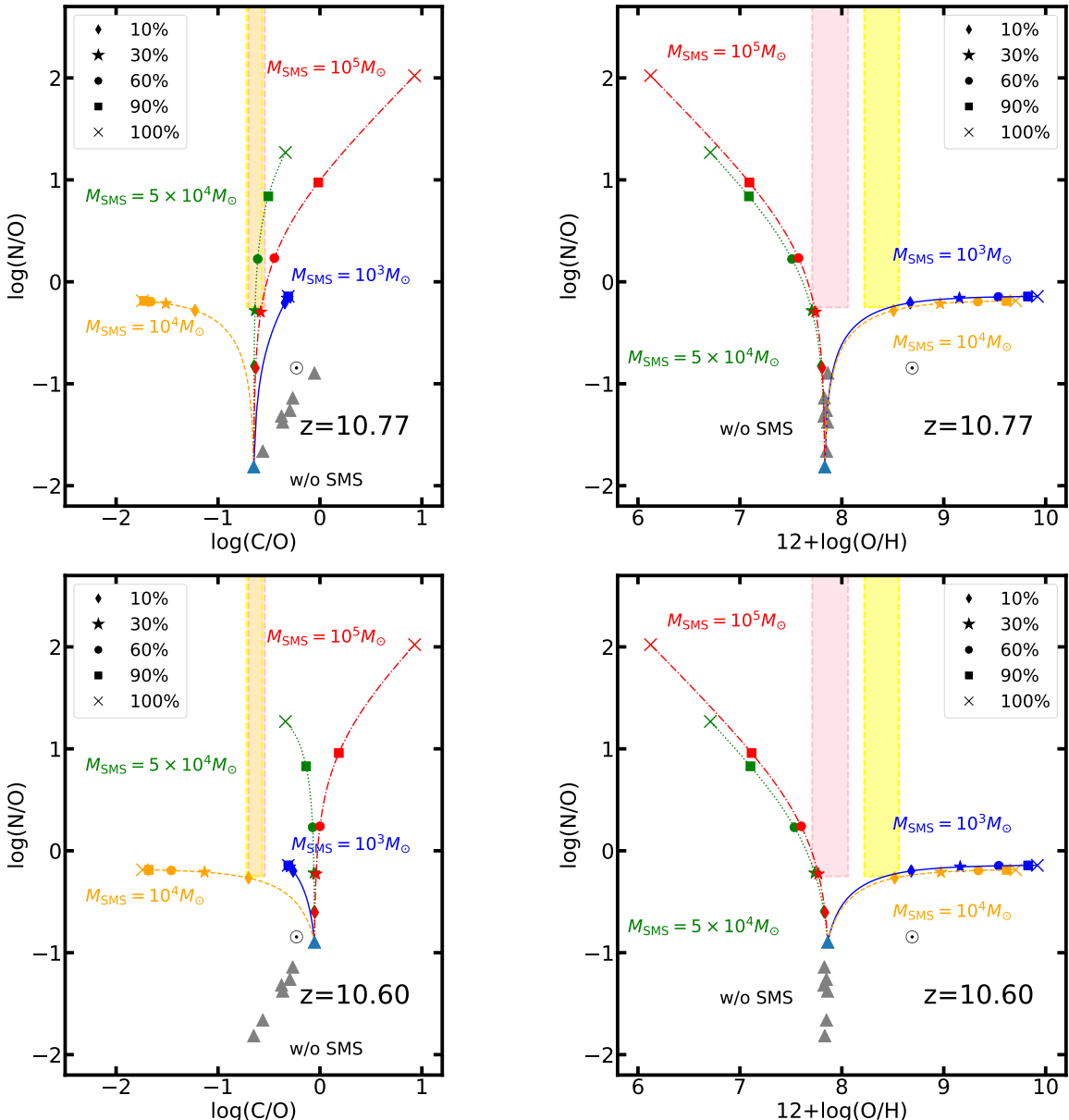


Fig. 6:  $\log(N/O)$  as a function of  $\log(C/O)$  (left) and  $12 + \log(O/H)$  (right). The gray triangles indicate the chemical abundance of our simulated galaxy without SMS pollution between  $z = 10.77$  and  $10.60$ . In the top two panels, the blue triangle indicates  $z = 10.77$ . In contrast, in the bottom two panels, the blue triangle represents  $z = 10.60$ . We added SMS ejecta for these two different time. The blue solid, yellow dashed, green dotted, and red dash-dotted indicate the abundance ratio for  $10^3 M_\odot$ ,  $10^4 M_\odot$ ,  $5 \times 10^4 M_\odot$ , and  $10^5 M_\odot$  SMSs, respectively. The symbols (rhombus, star, circle, square, and cross) indicate the pollution fraction ( $f_{\text{SMS}}$ ) of 10, 30, 60, 90, and 100 per cent. The pink shaded region indicates the chemical abundance of GN-z11 combined  $\log(N/O)$  value of Cameron et al. (2023) and  $\log(C/O)$  and  $\log(O/H)$  value from Isobe et al. (2025) with an electron number density  $n_e = 10^3 \text{ cm}^{-3}$ . The yellow shaded region represents the GN-z11's abundance from  $\log(N/O)$  in Cameron et al. (2023) and  $\log(C/O)$  and  $\log(O/H)$  from Isobe et al. (2025) with  $n_e = 10^5 \text{ cm}^{-3}$ . The solar symbol represents the solar abundance (Asplund et al. 2021).

bination coefficient (Tielens 2005):

$$\alpha = 2.56 \times 10^{-13} \times (T/10^4 \text{ K})^{-0.83} [\text{cm}^3 \text{ s}^{-1}].$$

To calculate the Strömgren radius, we need  $n_H$  and  $Q$ . One may think that we can obtain  $n_H$  from the simulation, but the softening length for the baryons in our simulation is  $\sim 6$  pc, so that we cannot resolve the gas distribution at the innermost region. We, therefore, assume a uniform density of the gas;  $n_H = 10^3$ ,  $10^4$ , and  $10^5 \text{ cm}^{-3}$ , considering uncertainties. As shown in Fig. 5, the central gas density in our simulation was  $\sim 10^4 M_\odot \text{ pc}^{-3}$ ,

i.e.,  $\sim 10^5 \text{ cm}^{-3}$ . On the other hand, recent JWST observations suggested that electron densities of  $10^3 \text{ cm}^{-3}$  for galaxies at  $z \sim 10$  (Abdurro'uf et al. 2024). We therefore set these values as higher and lower limits.

We estimated  $Q$  using the effective temperature obtained from the  $10^4 M_\odot$  SMS model;  $T_{\text{eff}} = 7.09 \times 10^4 \text{ K}$  (the maximum value) (see Section 2.2). The value of  $Q$  was calculated with

$$Q = 4\pi R^2 \int \int_{h\nu=13.6 \text{ eV}}^{\infty} \frac{B(\nu, T_{\text{eff}})}{h\nu} \cos \theta d\nu d\Omega,$$

Table 3: The Strömgren radius and gas mass inside the Strömgren sphere under the different gas number density. Note that gas density was assumed to be uniform.

| $n_{\text{H}}$ [cm $^{-3}$ ] | $R_{\text{S}}$ [pc]   | $M_{\text{S}}$ [M $_{\odot}$ ] | $f_{\text{SMS}}$ [per cent] |
|------------------------------|-----------------------|--------------------------------|-----------------------------|
| 10 $^3$                      | 16.4                  | 4.59 $\times 10^5$             | 0.99                        |
| 10 $^4$                      | 3.54                  | 4.59 $\times 10^4$             | 9.09                        |
| 10 $^5$                      | 7.63 $\times 10^{-1}$ | 4.59 $\times 10^3$             | 50                          |

where  $R$  is radius of the SMS,  $T_{\text{eff}}$  is an effective temperature, and  $B(v, T_{\text{eff}})$  is the Planck's law (Planck 1901). Using the maximum effective temperature ( $T_{\text{eff}} = 7.09 \times 10^4$  K) and the radius at this moment ( $R = 124 R_{\odot}$ ), we obtained  $Q = 2.68 \times 10^{52}$  s $^{-1}$ . The resultant Strömgren radius,  $R_{\text{S}}$ , and the mass within the radius,  $M_{\text{S}}$ , are

$$R_{\text{S}} = 1.63 \times 10^3 \times \left( \frac{n_{\text{H}}}{1 \text{ cm}^{-3}} \right)^{-2/3} \text{ [pc]}, \quad (4)$$

and

$$M_{\text{S}} = 4.59 \times 10^8 \times \left( \frac{n_{\text{H}}}{\text{cm}^{-3}} \right)^{-1} \text{ [M}_{\odot}\text]}, \quad (5)$$

respectively. In Table 3, we summarized  $R_{\text{S}}$  and  $M_{\text{S}}$ , for each given  $n_{\text{H}}$ . The higher the gas density, the higher the pollution fraction (see Table 3). From these results, we found that  $f_{\text{SMS}} = 10\text{--}30$  per cent can be obtained from  $n_{\text{H}} = 10^4\text{--}10^5$  cm $^{-3}$ .

On the other hand, the 10 $^5$  M $_{\odot}$  SMS model causes an explosion (see Table 1). We also estimate the radius of the supernovae shell ( $R_{\text{SNR}}$ ) using the estimation given in Cioffi et al. (1988):

$$R_{\text{SNR}} = 69.02 \times \left( \frac{E_{\text{explosion}}}{10^{51} \text{ erg}} \right)^{31/98} \times \left( \frac{n_{\text{H}}}{1 \text{ cm}^{-3}} \right)^{-18/49} \times \xi_{\text{m}}^{-5/98} \times \beta^{-3/7} \times \left( \frac{c_0}{10 \text{ km s}^{-1}} \right)^{-3/7} \text{ [pc]}, \quad (6)$$

where  $E_{\text{explosion}}$  is an explosion energy,  $c_0$  is a sound speed,  $\xi_{\text{m}}$  is a metallicity factor, and  $\beta$  is an index. By fixing  $c_0 = 10 \text{ km s}^{-1}$ ,  $\beta = 1$  and  $\xi_{\text{m}} = 1$ , we obtained  $R_{\text{SNR}} = 17.2\text{--}93.6$  pc and enclosed gas mass  $5 \times 10^7\text{--}8 \times 10^7$  M $_{\odot}$  for  $n_{\text{H}} = 10^3\text{--}10^5$  cm $^{-3}$ . If ejecta were fully mixed with the gas inside the shell, the pollution fraction is only  $\sim 10^{-1}$  per cent. In the 10 $^5$  M $_{\odot}$  SMS case, the shock wave swept a large amount of gas, and therefore, pollution cannot be dominant.

## 4. Discussion

### 4.1. Other high- $z$ N/O-enhanced galaxies

Not only GN-z11, but several N/O-enhanced galaxies have been found. We also compared their abundance patterns to our SMS models. For observational data, we used N/O-enhanced galaxies summarized in Ji et al. (2025), but for  $z \gtrsim 6$ , which is  $\lesssim 1$  Gyr, and therefore we expect less AGB pollution. We also included MoM-z14 (Naidu et al. 2025). The results are shown in Fig. 7. The N/O is mostly higher than the solar abundance, and three of ten have N/O as high as that of GN-z11. The C/O of these galaxies is lower than the solar abundance and mostly lower than that of GN-z11. Their O/H is also subsolar and comparable to or lower than that of GN-z11. There is no clear redshift dependence.

For their C/O values even lower than that of GN-z11, our 10 $^4$  M $_{\odot}$  SMS model that produces lower C/O or massive SMS models ( $5 \times 10^4$  and 10 $^5$  M $_{\odot}$ ) with low C/O of galactic gas ( $z = 10.77$ ) is preferable (see the left panels of Fig. 7). For their O/H values lower than that of GN-z11, our 5  $\times 10^4$  and 10 $^5$  M $_{\odot}$  SMS models are preferable (see the right panels of Fig. 7). However, a lower O/H can be realized with a slightly lower O/H of the gas without SMS. The O/H ratio here is determined by the gas accreting from the outside of this galaxy, and the O/H ratio reflects the pollution history from Pop-III and II stars and their ejecta. Therefore, the O/H ratio we adopted here (12+log (O/H) = 7.82) may also differ if the galaxy has a slightly different formation history. In addition, the abundance pattern of the SMS ejecta does not sequentially change with the SMS mass in our models. Therefore, other SMS mass models may also cover the abundance patterns of the N/O-enhanced galaxies.

### 4.2. Helium abundance

Not only C, N, O, and H, but also helium (He) abundances of N/O-enhanced galaxies, including GN-z11, have been measured (Yanagisawa et al. 2024; Ji et al. 2025). In Fig. 8, we present the helium abundances of the N/O-enhanced galaxies (Ji et al. 2025). We note that some of the galaxies in Ji et al. (2025) lack measured helium abundances.

In Fig. 8, we present the He/H of our models ( $z = 10.77\text{--}10.60$ ) and observed ones as functions of N/O (the left panel) and O/H (the right panel), respectively. We added SMS ejecta to our  $z = 10.65$  result, since the He/H does not largely change in the  $z$  range we adopted (see Table 2). The He/H in our simulation was consistent with that observed in the N/O-enhanced galaxies and GN-z11 without SMS pollution. The He/H increases with SMS pollution but remains low compared to GN-z11 when the pollution fraction is  $\lesssim 10\text{--}30$  per cent, depending on the SMS mass.

For the other galaxies, there are only three N/O-enhanced samples because we limited the redshift to  $z > 6$ . The He/H of them is comparable to or higher than that of GN-z11. Such He/H can be explained by the SMS pollution. Yanagisawa et al. (2024) reported an anti-correlation between N/O and He/H, and Ji et al. (2025) discussed that there is an anti-correlation between He/H and O/H and that such an anti-correlation can be explained by the SMS scenario. The correlation between O/H and He/H can be reproduced by the SMS pollution. The anti-correlation can also be achieved for massive SMSs ( $5 \times 10^4$  and 10 $^5$  M $_{\odot}$ ).

## 5. Summary

To understand the formation mechanism of N/O-enhanced high- $z$  galaxies such as GN-z11, we performed a post-processing analysis on chemical evolution using a cosmological zoom-in  $N$ -body/SPH simulation of a GN-z11-like galaxy. Although the simulation includes chemical enrichment due to WR and AGB stars, the N/O ratio of the formed galaxy was lower than that of GN-z11. As a post-process, we considered pollution from SMSs. From a previous numerical study on the formation of VMSs/SMSs in forming star clusters (Fujii et al. 2024), we assumed 3–5 per cent of the forming stellar mass in the central 10 pc of the galaxy contributes to the SMS mass at the galactic center. With the star formation rate of the central 10 pc obtained from our simulation, we estimated that an SMS with 10 $^{3\text{--}5}$  M $_{\odot}$  can be formed in our simulated galaxy.

Assuming that all the ejecta from the SMS are mixed with the gas in the HII region irradiated by the SMS, we calculated the

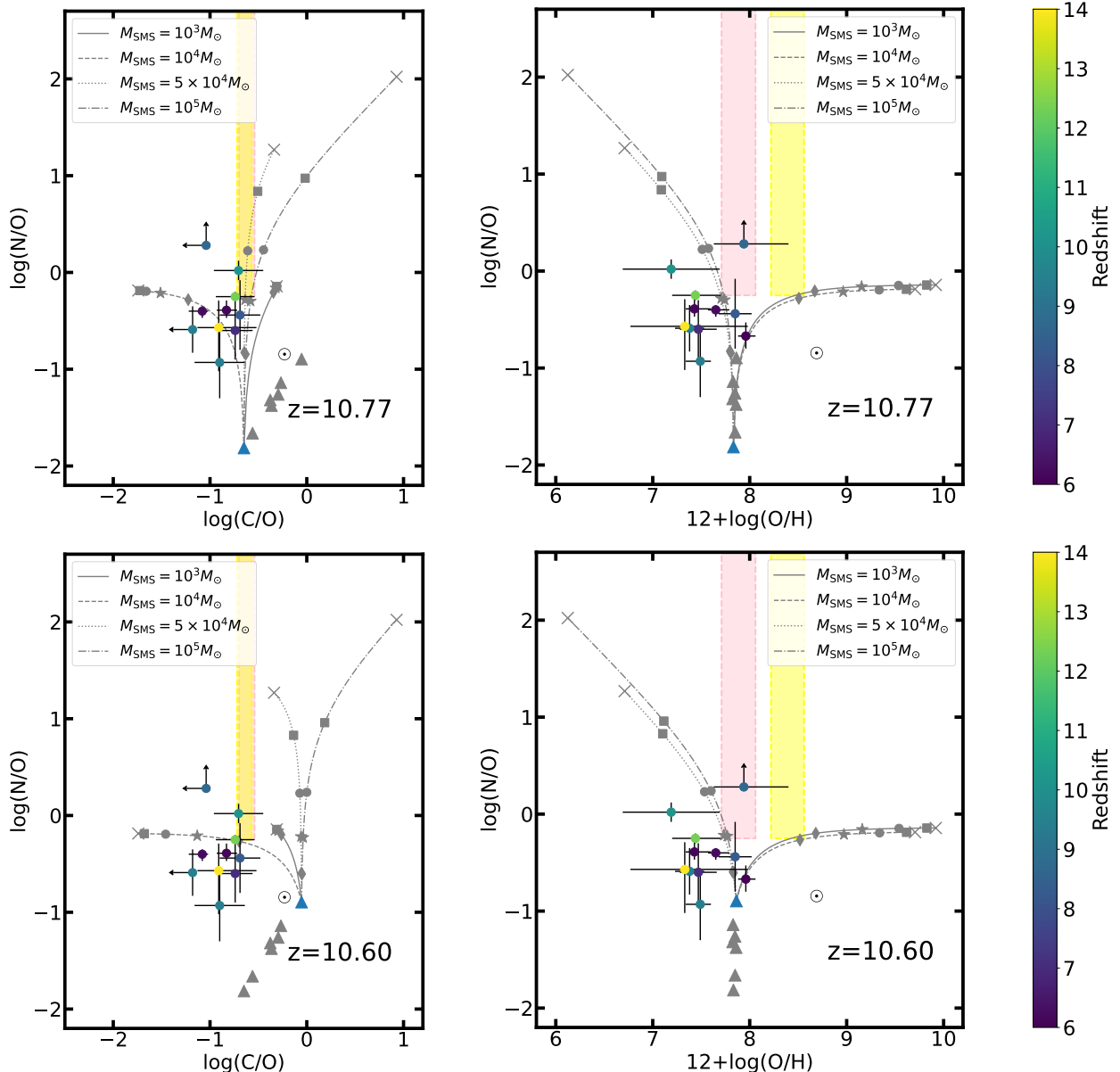


Fig. 7: Same as Fig. 6 but comparison with the N/O-enhanced galaxies with  $z \gtrsim 6$  in Table 2 (colored circles with error bars). The marker color varies according to their redshifts in the range of  $6 \leq z \leq 14$ . Gray curves indicate our results for  $10^3$  (solid),  $10^4$  (dashed),  $5 \times 10^4$  (dotted), and  $10^5$  (dash-dotted)  $M_\odot$  SMSs. The symbols (rhombus, star, circle, square, and cross) indicate the pollution fraction ( $f_{\text{SMS}}$ ) of 10, 30, 60, 90, and 100 per cent. The color-shaded regions indicate the abundance ratios of GN-z11.

abundance ratios with SMS pollution. The high N/O ratio of GN-z11 can be obtained by the SMS pollution. The abundance pattern changes with the SMS masses (Nagele & Umeda 2023). For our simulated galaxy, the yields from the  $10^4$ – $10^5 M_\odot$  SMS models with the pollution fraction of 10–30 per cent reproduced the observed abundance ratio of GN-z11. Such a pollution fraction can be achieved assuming the gas with  $10^4$ – $10^5 \text{ cm}^{-3}$  ionized by the SMS. The He/H obtained from our models is also consistent with that of GN-z11.

Additionally, we compared our results with other N/O-enhanced galaxies. The N/O-enhanced galaxies show lower C/O ratios than GN-z11; these can be explained best by our  $10^4 M_\odot$  SMS model. On the other hand, our  $\gtrsim 5 \times 10^4 M_\odot$  SMS models are preferable for the low O/H of the N/O-enhanced galaxies, but a slightly different galaxy formation history may be able to achieve a lower O/H or lower C/O than our current galaxy model.

Similar to the N/O-enhanced galaxies, globular clusters exhibit N/O-enhanced features (Charbonnel et al. 2023; Senchyna et al. 2024; Ji et al. 2025). VMS formation via runaway collision of stars (Fujii et al. 2024) and pollution may also work in globular clusters.

**Acknowledgements.** We thank Chihong Lin and John Silverman for helpful discussions. The numerical simulation was carried out on the GPU system XD2000 at the Center for Computational Astrophysics (CfCA) at National Astronomical Observatory of Japan (NAOJ). The analysis was also done by the analysis server at CfCA. Sho Ebihara was supported by Forefront Physics and Mathematics Program to Drive Transformation (FoPM), a World-leading Innovative Graduate Study (WINGS) Program, hosted by the University of Tokyo. This study is supported by JSPS KAKENHI Grant No. 24KJ0202, 23K22530, 21K03614, 21K03633, 22KJ0157, 22K03688, 24K07095, 25K01046, and 25H00664.

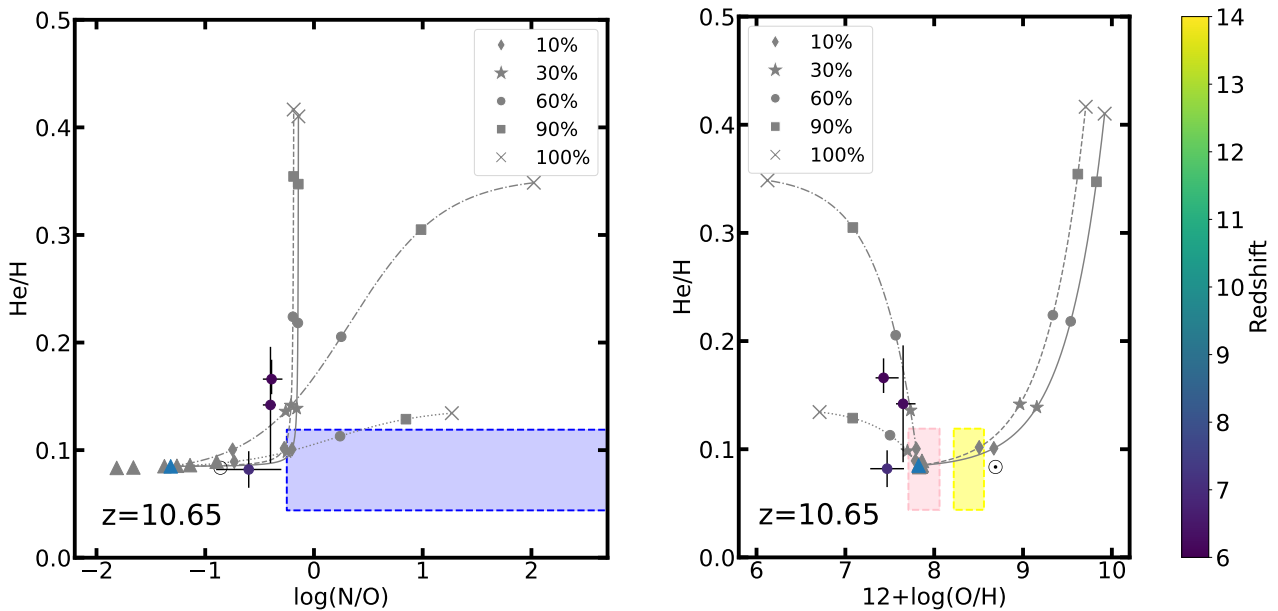


Fig. 8: Abundance patterns of N/O-He/H (left) and O/H-He/H (right). Colored-circle markers are the same as Fig. 7 but only for the N/O-enhanced galaxies for which the He/H are given. gray curves indicate our results ( $z = 10.65$ ) for  $10^3$  (solid),  $10^4$  (dashed),  $5 \times 10^4$  (dotted), and  $10^5$  (dash-dotted)  $M_{\odot}$  SMS models. The solar abundance is shown by the solar symbol. The blue shaded region indicates the GN-z11's value from Cameron et al. (2023) and Ji et al. (2025). The pink and yellow-shaded regions are also the same as Fig. 7, but we adopted the He/H value from Ji et al. (2025).

## References

Abdurro'uf, Larson, R. L., Coe, D., et al. 2024, ApJ, 973, 47  
 Álvarez-Márquez, J., Crespo Gómez, A., Colina, L., et al. 2025, A&A, 695, A250  
 Asplund, M., Amarsi, A. M., & Grevesse, N. 2021, A&A, 653, A141  
 Asplund, M., Grevesse, N., Sauval, A. J., & Scott, P. 2009, ARA&A, 47, 481  
 Barnes, J. & Hut, P. 1986, Nature, 324, 446  
 Berg, D. A., Erb, D. K., Henry, R. B. C., Skillman, E. D., & McQuinn, K. B. W. 2019, ApJ, 874, 93  
 Berg, D. A., Skillman, E. D., Henry, R. B. C., Erb, D. K., & Carigi, L. 2016, ApJ, 827, 126  
 Bunker, A. J., Cameron, A. J., Curtis-Lake, E., et al. 2024, A&A, 690, A288  
 Bunker, A. J., Saxena, A., Cameron, A. J., et al. 2023, A&A, 677, A88  
 Calabro, A., Castellano, M., Zavala, J. A., et al. 2024, ApJ, 975, 245  
 Cameron, A. J., Katz, H., Rey, M. P., & Saxena, A. 2023, MNRAS, 523, 3516  
 Castellano, M., Napolitano, L., Fontana, A., et al. 2024, ApJ, 972, 143  
 Chabrier, G. 2003, PASP, 115, 763  
 Chandrasekhar, S. 1964, ApJ, 140, 417  
 Charbonnel, C., Schaerer, D., Prantzos, N., et al. 2023, A&A, 673, L7  
 Chon, S., Hosokawa, T., & Yoshida, N. 2018, MNRAS, 475, 4104  
 Cioffi, D. F., McKee, C. F., & Bertschinger, E. 1988, ApJ, 334, 252  
 Cristallo, S., Piersanti, L., & Straniero, O. 2016, in Journal of Physics Conference Series, Vol. 665, Journal of Physics Conference Series (IOP), 012019  
 Cristallo, S., Straniero, O., & Piersanti, L. 2014, in XIII Nuclei in the Cosmos (NIC XIII), 81  
 Cristallo, S., Straniero, O., & Piersanti, L. 2015, in Astronomical Society of the Pacific Conference Series, Vol. 497, Why Galaxies Care about AGB Stars III: A Closer Look in Space and Time, ed. F. Kerschbaum, R. F. Wing, & J. Hron, 301  
 Curti, M., Witstok, J., Jakobsen, P., et al. 2025, A&A, 697, A89  
 D'Antona, F., Vesperini, E., Calura, F., et al. 2023, A&A, 680, L19  
 Devecchi, B. & Volonteri, M. 2009, ApJ, 694, 302  
 Domínguez, I., Cristallo, S., Straniero, O., et al. 2011, in Astronomical Society of the Pacific Conference Series, Vol. 445, Why Galaxies Care about AGB Stars II: Shining Examples and Common Inhabitants, ed. F. Kerschbaum, T. Lebzelter, & R. F. Wing, 57  
 Ferland, G. J., Porter, R. L., van Hoof, P. A. M., et al. 2013, Rev. Mexicana Astron. Astrofis., 49, 137  
 Fukui, M. S., Wang, L., Tanikawa, A., Hirai, Y., & Saitoh, T. R. 2024, Science, 384, 1488  
 Fukushima, K., Nagamine, K., Matsumoto, A., et al. 2025, ApJ, 988, 46  
 Gieles, M., Charbonnel, C., Krause, M. G. H., et al. 2018, MNRAS, 478, 2461  
 Gunawardhana, M. L. P., Brinchmann, J., Croom, S., et al. 2025, MNRAS [arXiv:2504.12584]  
 Haardt, F. & Madau, P. 2012, ApJ, 746, 125  
 Haemmerlé, L., Meynet, G., Mayer, L., et al. 2019, A&A, 632, L2  
 Hahn, O. & Abel, T. 2011, MNRAS, 415, 2101  
 Hirai, Y. & Saitoh, T. R. 2017, ApJ, 838, L23  
 Hirano, S., Machida, M. N., & Basu, S. 2021, ApJ, 917, 34  
 Hopkins, P. F., Wetzel, A., Kereš, D., et al. 2018, MNRAS, 477, 1578  
 Incacolciato, A., Khochfar, S., & Oñorbe, J. 2023, MNRAS, 522, 330  
 Isobe, Y., Maiolino, R., Ji, X., et al. 2025, arXiv e-prints, arXiv:2509.18055  
 Isobe, Y., Ouchi, M., Tominaga, N., et al. 2023, ApJ, 959, 100  
 Izotov, Y. I., Stasińska, G., Meynet, G., Guseva, N. G., & Thuan, T. X. 2006, A&A, 448, 955  
 Ji, X., Belokurov, V., Maiolino, R., et al. 2025, arXiv e-prints, arXiv:2505.12505  
 Latif, M. A., Khochfar, S., Schleicher, D., & Whalen, D. J. 2021, MNRAS, 508, 1756  
 Latif, M. A., Schleicher, D. R. G., Bovino, S., Grassi, T., & Spaans, M. 2014, ApJ, 792, 78  
 Limongi, M. & Chieffi, A. 2018, ApJS, 237, 13  
 Maiolino, R., Scholtz, J., Witstok, J., et al. 2024a, Nature, 627, 59  
 Maiolino, R., Übler, H., Perna, M., et al. 2024b, A&A, 687, A67  
 McClymont, W., Tacchella, S., Smith, A., et al. 2025, arXiv e-prints, arXiv:2507.08787  
 Nagele, C. & Umeda, H. 2023, ApJ, 949, L16  
 Nagele, C. & Umeda, H. 2024, Phys. Rev. D, 110, L061301  
 Nagele, C., Umeda, H., & Takahashi, K. 2023, MNRAS, 523, 1629  
 Nagele, C., Umeda, H., Takahashi, K., Yoshida, T., & Sumiyoshi, K. 2020, MNRAS, 496, 1224  
 Nagele, C., Umeda, H., Takahashi, K., Yoshida, T., & Sumiyoshi, K. 2022, MNRAS, 517, 1584  
 Naidu, R. P., Oesch, P. A., Brammer, G., et al. 2025, arXiv e-prints, arXiv:2505.11263  
 Nandal, D., Regan, J. A., Woods, T. E., et al. 2024, A&A, 683, A156  
 Napolitano, L., Castellano, M., Pentericci, L., et al. 2025, ApJ, 989, 75  
 Navarro-Carrera, R., Caputi, K. I., Iani, E., et al. 2024, arXiv e-prints, arXiv:2407.14201  
 Nomoto, K., Kobayashi, C., & Tominaga, N. 2013, ARA&A, 51, 457  
 Oesch, P. A., Brammer, G., van Dokkum, P. G., et al. 2016, ApJ, 819, 129  
 Pacucci, F., Hernquist, L., & Fujii, M. 2025, arXiv e-prints, arXiv:2509.02664  
 Pilyugin, L. S., Vilchez, J. M., Mattsson, L., & Thuan, T. X. 2012, MNRAS, 421, 1624  
 Planck, M. 1901, Annalen der Physik, 309, 553  
 Planck Collaboration, Aghanim, N., Akrami, Y., et al. 2020, A&A, 641, A6  
 Portegies Zwart, S. F. & McMillan, S. L. W. 2002, ApJ, 576, 899  
 Rantala, A., Naab, T., & Lahén, N. 2024, MNRAS, 531, 3770

Rizzuti, F., Matteucci, F., Molaro, P., Cescutti, G., & Maiolino, R. 2025, A&A, 697, A96

Saitoh, T. R. 2017, AJ, 153, 85

Saitoh, T. R., Daisaka, H., Kokubo, E., et al. 2008, PASJ, 60, 667

Saitoh, T. R., Daisaka, H., Kokubo, E., et al. 2009, PASJ, 61, 481

Saitoh, T. R., Hirai, Y., Fujii, M. S., & Isobe, Y. 2025, arXiv e-prints, arXiv:2511.23164

Saitoh, T. R. & Makino, J. 2013, ApJ, 768, 44

Saitoh, T. R. & Makino, J. 2016, ApJ, 823, 144

Sakurai, Y., Yoshida, N., Fujii, M. S., & Hirano, S. 2017, MNRAS, 472, 1677

Schaerer, D., Marques-Chaves, R., Xiao, M., & Korber, D. 2024, A&A, 687, L11

Scholtz, J., Witten, C., Laporte, N., et al. 2024, A&A, 687, A283

Seitenzahl, I. R., Ciaraldi-Schoolmann, F., Röpke, F. K., et al. 2013, MNRAS, 429, 1156

Senchyna, P., Plat, A., Stark, D. P., et al. 2024, ApJ, 966, 92

Shen, S., Wadsley, J., & Stinson, G. 2010, MNRAS, 407, 1581

Smith, B. D., Bryan, G. L., Glover, S. C. O., et al. 2017, MNRAS, 466, 2217

Stiavelli, M., Morishita, T., Chiaberge, M., et al. 2025, ApJ, 981, 136

Strömgren, B. 1939, ApJ, 89, 526

Susa, H., Hasegawa, K., & Tominaga, N. 2014, ApJ, 792, 32

Tacchella, S., Eisenstein, D. J., Hainline, K., et al. 2023, ApJ, 952, 74

Takahashi, K., Sumiyoshi, K., Yamada, S., Umeda, H., & Yoshida, T. 2019, ApJ, 871, 153

Takahashi, K., Yoshida, T., & Umeda, H. 2018, ApJ, 857, 111

Takahashi, K., Yoshida, T., Umeda, H., Sumiyoshi, K., & Yamada, S. 2016, MNRAS, 456, 1320

Tielens, A. G. G. M. 2005, The Physics and Chemistry of the Interstellar Medium (Cambridge University Press)

Topping, M. W., Stark, D. P., Senchyna, P., et al. 2025, ApJ, 980, 225

Topping, M. W., Stark, D. P., Senchyna, P., et al. 2024, MNRAS, 529, 3301

Vink, J. S. 2018, A&A, 615, A119

Watanabe, K., Ouchi, M., Nakajima, K., et al. 2024, ApJ, 962, 50

Xu, Y., Ouchi, M., Yajima, H., et al. 2024, ApJ, 976, 142

Yamada, S. 1997, ApJ, 475, 720

Yanagisawa, H., Ouchi, M., Watanabe, K., et al. 2024, ApJ, 974, 266

Yoshida, T., Takiwaki, T., Kotake, K., et al. 2019, ApJ, 881, 16

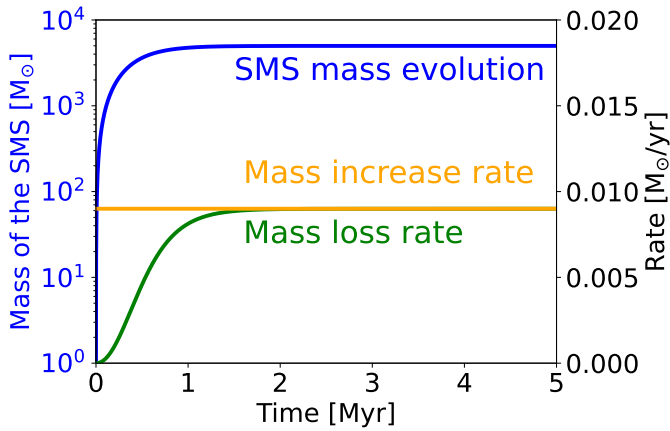


Fig. A.1: Mass evolution of SMS (blue curve) when a mass increase rate was minimum value,  $9 \times 10^{-3} M_{\odot} \text{ yr}^{-1}$  (orange line) and metallicity of  $0.1 Z_{\odot}$ . The green curve indicates the mass loss rate calculated with Eq. 1 (Vink 2018).

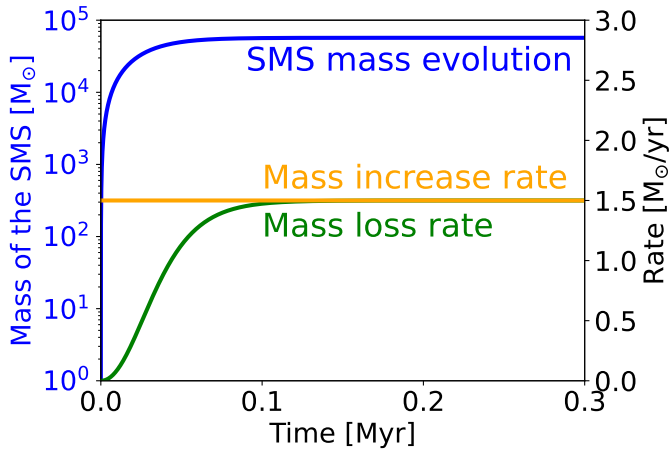


Fig. A.2: Same as Fig. A.1, mass evolution of SMS when a mass increase rate was maximum value,  $1.5 M_{\odot} \text{ yr}^{-1}$ .

\*

## Appendix A: SMS mass estimation

Although we estimated the SMS mass that can form in the galaxy from the SFR of the galactic center, there would be an uncertainty in the SMS mass. As we discussed in Sec 3.2, the mass increase rate had an uncertainty between  $9 \times 10^{-3} M_{\odot} \text{ yr}^{-1}$  and  $1.5 M_{\odot} \text{ yr}^{-1}$ . Fixing the mass-loss rate of Eq. 1, we obtained  $5.0 \times 10^3 M_{\odot}$  (see Fig. A.1). The formation timescale is  $\sim 1$  Myr. Similarly, we also estimated the maximum mass. With 5 per cent of  $30 M_{\odot} \text{ yr}^{-1}$ , i.e.  $1.5 M_{\odot} \text{ yr}^{-1}$ , we estimated  $5.7 \times 10^4 M_{\odot}$  as the upper limit of the SMS mass (see Fig. A.2). The formation time is only 0.1 Myr. From these results, we assumed the mass of SMS formed at the galactic center would be in the range of  $10^{3-5} M_{\odot}$ .

## Appendix B: Variation in the abundance ratios in different snapshots

In N/O vs. He/H plot and O/H vs. He/H plot (See the Fig. 8), we added SMS ejecta to our  $z = 10.65$  result because no matter

which snapshot ( $z = 10.77-10.60$ ) we added the ejecta to, the result do not change. As proof, we show N/O vs. He/H plot and O/H vs. He/H plot in Fig. B.1. We added SMS ejecta to our  $z = 10.77$  result (the top two panels), and our  $z = 10.60$  result (the bottom two panels). Since He/H and O/H does not change significantly, the region SMS model pass by does not change regardless of redshifts.

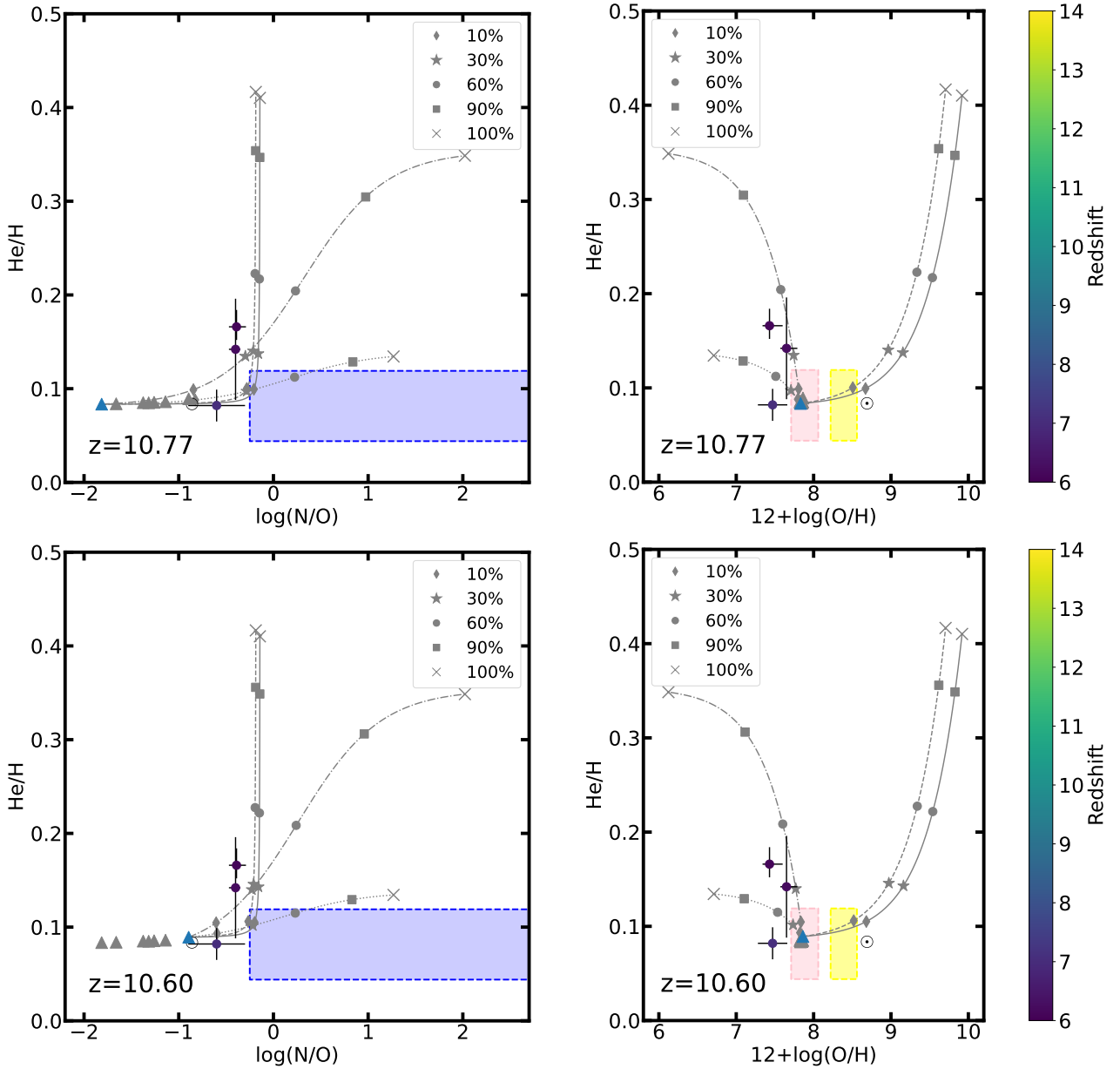


Fig. B.1: Same as Fig. 8, we show N/O vs. He/H and O/H vs. He/H plot for our results and reported N/O-enhanced galaxies. The results we added SMS ejecta to our  $z = 10.77$  snapshot (the blue triangle) are shown in top two panels. The bottom two panels are results for our  $z = 10.60$  snapshot (the blue triangle). For the reference, the chemical abundance at other snapshot  $z = 10.77$ – $10.60$  are plotted by gray triangles.